



Cite this: *Catal. Sci. Technol.*, 2023, 13, 5248

## Co-activation of methane and nitrogen to acetonitrile over $\text{MoC}_x/\text{Al}_2\text{O}_3$ catalysts†

Korawich Trangwachirachai, <sup>a</sup> I-Ting Kao, <sup>a</sup> Wei-Hsiang Huang, <sup>b</sup> Chi-Liang Chen <sup>b</sup> and Yu-Chuan Lin <sup>a\*</sup>

Methane and nitrogen are regarded as the most abundant sources of hydrocarbons and nitrogen, respectively. Both compounds exhibit high stability due to the presence of daunting C–H and N≡N bond energies of 439 and 945 kJ mol<sup>−1</sup>, respectively, leading to their abundance. This study investigates the co-activation of methane and nitrogen using  $\text{Al}_2\text{O}_3$ -supported  $\text{MoC}_x$  catalysts (1, 5, and 10 wt%) to produce acetonitrile (ACN) at ambient pressure. It was found that the optimum methane conversion (26.1%) and turnover frequency (TOF) of ACN (15.3 h<sup>−1</sup>) were achieved at 750 °C using 1 wt% Mo loading. To alleviate catalyst deactivation resulting from coking, H<sub>2</sub> co-feeding was implemented and found to effectively sustain the on-stream activity for 50 hours. A plausible mechanism for ACN production, which occurs on the MoC-like surface, was proposed.

Received 28th April 2023,  
Accepted 4th August 2023

DOI: 10.1039/d3cy00585b

rsc.li/catalysis

## Introduction

Methane ( $\text{CH}_4$ ), the major component of natural gas, shale gas, and biogas, has long been used as a heat resource by combustion.<sup>1</sup> Because of its abundance,  $\text{CH}_4$  is considered an important building block in the production of value-added chemicals.<sup>2,3</sup> For example,  $\text{CH}_4$  can be converted to syngas (CO and H<sub>2</sub>) by steam or dry reforming<sup>4–7</sup> and further converted to hydrocarbons by Fischer–Tropsch synthesis.<sup>8,9</sup>  $\text{CH}_4$  can also be converted to olefins, aromatics, or oxygenated compounds (e.g., formaldehyde and methanol) by non-oxidative pyrolysis, dehydroaromatization, or selective partial oxidation.<sup>9–11</sup> However, the chemical inertness and high C–H bond dissociation energy of  $\text{CH}_4$  hinder its conversion to chemicals.<sup>9</sup> Fig. 1 shows the existing routes for catalytic  $\text{CH}_4$  conversion, including  $\text{CH}_4$  to olefins, aromatics, and hydrogen (MTO, MTA, and MTOAH), oxidative coupling (OCM), and dehydroaromatization (MDA).

Besides the conventional reforming processes (e.g., steam and dry reforming), limited studies have been dedicated to the direct conversion of  $\text{CH}_4$  to chemicals through non-oxidative routes. McFarland *et al.* reported the production of H<sub>2</sub> and solid carbon derived from  $\text{CH}_4$  catalyzed by molten metal alloys.<sup>12</sup> The catalysts were prepared by

dissolving active metals (Ni, Pd, and Pt) in low-melting-temperature metal solvents (Sn, Pb, Bi, In, and Ga) at temperatures below 1000 °C. 27 mol% Ni in Bi was the most active catalyst, achieving a  $1.7 \times 10^{-8}$  mol<sub>H<sub>2</sub></sub> cm<sup>−2</sup> s<sup>−1</sup> hydrogen production rate with more than 95% selectivity at 950 °C. The Kopyscinski group studied silica-supported GaN prepared by ammonia nitridation for  $\text{CH}_4$  conversion to ethylene.<sup>13</sup> They found that  $\text{CH}_4$  can be converted to ethylene at above 700 °C. Our group recently discovered that GaN made by co-pyrolyzing gallium nitrate and organic nitrogen compounds (e.g., melamine, melem, and g-C<sub>3</sub>N<sub>4</sub>) could convert  $\text{CH}_4$  to acetonitrile (ACN).<sup>14,15</sup> The impact of particle size of GaN and residual CN species (including C≡N and C≡N) on the enhancement of ACN production was found to be significant. However, it is worth noting that the residual CN species cannot be regenerated during the conversion process and gradually get depleted.

Currently, ACN is obtained primarily as a by-product (approximately 2–4%) from acrylonitrile synthesis known as the Sohio process.<sup>16</sup> This results in a comparatively low ACN

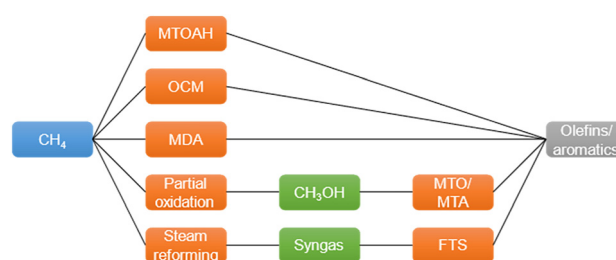


Fig. 1 Existing routes of  $\text{CH}_4$  conversion to chemicals.<sup>2</sup>

<sup>a</sup> Department of Chemical Engineering, National Cheng Kung University, Tainan 70101, Taiwan. E-mail: yclin768@mail.ncku.edu.tw

<sup>b</sup> National Synchrotron Radiation Research Center, Hsinchu 30076, Taiwan

† Electronic supplementary information (ESI) available: Time on stream (TOS) profiles and N<sub>2</sub> adsorption/desorption isotherms. See DOI: <https://doi.org/10.1039/d3cy00585b>

output that may not meet the escalating demand for ACN. In 2021, the global ACN market was valued at USD 264 million and is expected to grow at an annual rate of 5.5%.<sup>17</sup> Therefore, exploring alternative routes for ACN synthesis to meet the growing demand is needed. The advent of the shale gas revolution has led to a significant increase in natural gas production and a subsequent decline in CH<sub>4</sub> prices.<sup>18,19</sup> In 2017, the price of ACN in the United States was approximately nine times higher than that of CH<sub>4</sub>.<sup>20</sup> Accordingly, the conversion of CH<sub>4</sub> to ACN should be worth exploring.

Taking the Mars–van Krevelen redox cycle (Fig. 2) as an example,<sup>21</sup> the oxide catalyst delivers its mobile oxygen to partially oxidize the reactant to form an O-containing product, leaving the reduced catalyst in the first half of the cycle. Then, the reduced catalyst is re-oxidized by gaseous oxygen, fulfilling the redox cycle.

For the production of ACN *via* CH<sub>4</sub> conversion over supported GaN catalysts, only the first half of the redox cycle is completed. The addition of ammonia as a co-feed was expected to facilitate the remaining half of the cycle. However, the production of ACN was significantly reduced with even small amounts of co-fed NH<sub>3</sub> due to the *in situ* formed H<sub>2</sub> from NH<sub>3</sub> decomposition.<sup>14</sup> Therefore, using N<sub>2</sub> as a nitrogen source for ACN synthesis seems to be the most promising approach. In other words, a highly effective CH<sub>4</sub> conversion catalyst for ACN production must be capable of activating CH<sub>4</sub> and N<sub>2</sub> simultaneously. Tiwari *et al.* reported that CH<sub>4</sub> and N<sub>2</sub> could be activated simultaneously over a K-doped Ru catalyst to co-produce ammonia and ethylene.<sup>22</sup> The *in situ* H<sub>2</sub> produced from CH<sub>4</sub> conversion was used as a hydrogen source for ammonia synthesis. However, coke is formed in parallel with hydrogen production, resulting in discontinuous ammonia productivity. Nevertheless, this study introduces the possibility of converting two inert compounds into value-added chemicals.

The crucial step in N<sub>2</sub> activation is the cleavage of the N≡N bond. Mo<sub>2</sub>C has been demonstrated to be active in ammonia synthesis.<sup>23</sup> As predicted by the d-band model, transition metal carbides with vacant d orbitals exhibit

comparable adsorption behavior towards electron-rich adsorbates.<sup>24</sup> In addition, the sp bands of transition metals in metal carbides would hybridize with the d bands from the transition metals and with the s bands from the carbon.<sup>25</sup> The extra hybridized orbitals provide more opportunities for back-donation to the π orbitals of the adsorbates, making Mo<sub>2</sub>C a promising N<sub>2</sub> activation active site. Moreover, Mo<sub>2</sub>C was found as an active site in CH<sub>4</sub> dehydroaromatization.<sup>26–28</sup> Accordingly, the Mo<sub>2</sub>C catalyst should have strong potential for simultaneous activation of CH<sub>4</sub> (C–H) and N<sub>2</sub> (N≡N) to synthesize ACN.

In this study, the catalytic conversion of CH<sub>4</sub> and N<sub>2</sub> to ACN using Al<sub>2</sub>O<sub>3</sub>-supported MoC<sub>x</sub> catalysts was investigated. We found that the catalyst could simultaneously convert both CH<sub>4</sub> and N<sub>2</sub> to produce ACN. The optimum operating temperature and Mo loading were investigated. Catalyst deactivation was suppressed by introducing H<sub>2</sub> into the reaction stream, allowing the catalytic activity to be maintained for 50 h. In addition, a plausible mechanism for ACN formation was proposed to occur *via* the Mo-terminated MoC-like surface structure, which facilitates the reaction between CH<sub>4</sub> and N<sub>2</sub>. Kinetics analysis was performed to support the proposed mechanism, in which the surface reaction was suggested to be rate-limiting. The goal of this research is to validate the feasibility of converting two inert compounds (CH<sub>4</sub> and N<sub>2</sub>) into a valuable chemical (ACN).

## Experimental section

### Chemicals

Alumina (Al<sub>2</sub>O<sub>3</sub>, 99.5%), ammonium heptamolybdate ((NH<sub>4</sub>)<sub>6</sub>Mo<sub>7</sub>O<sub>24</sub>, 99.95%), molybdenum oxide (MoO<sub>3</sub>, 99.95%), and commercially available molybdenum carbide (com-Mo<sub>2</sub>C, 99.5%) were obtained from Merck, J. T. Baker, Alfa Aesar, and Sigma-Aldrich, respectively. CH<sub>4</sub> (99.999%), argon (Ar, 99.999%), nitrogen (N<sub>2</sub>, 99.999%), and hydrogen (H<sub>2</sub>, 99.999%) were purchased from Air Products. Al<sub>2</sub>O<sub>3</sub> was calcined at 750 °C before being used as a support. All chemicals were used as received.

### Catalyst preparation

Al<sub>2</sub>O<sub>3</sub>-supported MoC<sub>x</sub> catalysts were prepared by incipient-wetness impregnation followed by carbonization. Briefly, a designated amount of ammonium heptamolybdate solution (0.5 M) was added dropwise onto the Al<sub>2</sub>O<sub>3</sub> support to obtain xMo/Al<sub>2</sub>O<sub>3</sub> (x = 1, 5, or 10 wt%). The impregnated catalyst was dried at 110 °C overnight and was then calcined at 750 °C (5 °C min<sup>-1</sup>) for 5 h. Afterward, the calcined catalyst was sieved and crushed into 40–80 mesh particles. The carbonization treatment was performed before activity evaluation.

### Characterization

An inductively coupled plasma mass spectrometer (ICP-MS, THERMOELEMENT XR) was utilized to quantify the Mo

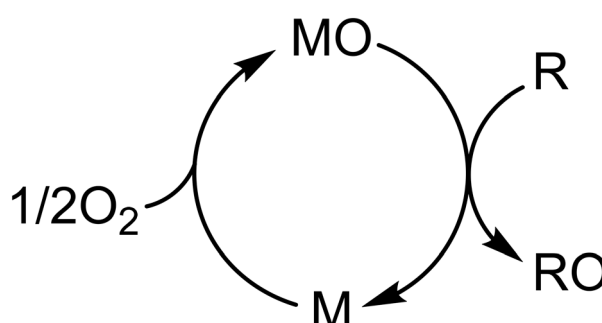


Fig. 2 Schematic illustration of the Mars–van Krevelen redox cycle, where MO is a metal oxide, M is the reduced form, R is a reactant, and RO is an O-containing product.

content. X-ray diffraction (XRD) patterns were recorded at 40 mA and 4 kV using a diffractometer (Rigaku D/Max-IIIB) equipped with Ni-filtered Cu K $\alpha$  ( $\lambda = 1.5406 \text{ \AA}$ ) radiation. A transmission electron microscope (TEM, JEOL JEM-2010) equipped with an energy dispersive X-ray spectrometer (EDS) was used to analyze the morphology of MoC<sub>x</sub> particles. N<sub>2</sub> sorption isotherms were analyzed using an automated physisorption analyzer (ASAP 2020 Plus, Micromeritics). The surface area was evaluated by applying the Brunauer–Emmett–Teller (BET) method at a relative pressure of 0.01–0.1.

X-ray absorption spectroscopy (XAS) at the Mo *K*-edge was performed at the Taiwan Photon Source (TPS) 44A beamline of the National Synchrotron Radiation Research Center (NSRRC), Taiwan. Mo-foil was used for energy calibration. The XAS spectra were analyzed by using the Athena and Artemis software ver. 0.9.26 included in the Demeter package.<sup>29</sup>

The CO pulse titration technique was conducted at 196 K to determine the dispersion of MoC<sub>x</sub> particles using a chemisorption analyzer (AutoChem II, Micromeritics) and the signals were recorded using a thermal conductivity detector (TCD). Ammonia and nitrogen temperature-programmed desorption (NH<sub>3</sub>- and N<sub>2</sub>-TPD) were conducted to determine the acidity and the N<sub>2</sub> desorption temperature, respectively, using the chemisorption analyzer. In a typical run, 0.2 g of catalyst was placed in a U-tube quartz reactor. The catalyst was then pretreated at 750 °C (10 °C min<sup>-1</sup>) for 30 min in a flow of Ar for dehydrating and outgassing. After cooling to 30 °C, the adsorbate (NH<sub>3</sub> or N<sub>2</sub>) was charged into the system for 1 h. After that, the sample was purged with He at 30 °C for 1 h to remove the excess gas. TPD was performed in a helium flow from 30 to 700 °C (10 °C min<sup>-1</sup>). *In situ* Fourier transform infrared (FTIR) spectra were recorded by using a Thermo Scientific Nicolet iS50 spectrometer equipped with a diffuse reflectance infrared Fourier transform spectroscopy cell (DRIFTS, Praying Mantis, Harrick Scientific). X-ray photoelectron spectroscopy (XPS) spectra were evaluated by using a PHI 5000 VersaProbe spectrometer equipped with a monochromatized aluminum source with a wavelength of 1486.6 eV. The tested samples were placed in a transport chamber from a glove box to the XPS chamber for quasi-*in situ* analysis to avoid air exposure. The C 1s binding energy of adventitious carbon at 285.0 eV was used to calibrate the energy shift.

### Catalytic activity testing

Activity tests were conducted in a horizontal fixed-bed flow reactor. In a typical run, 0.18 g of tested catalyst (no diluent) was sandwiched with quartz wool in the middle of a quartz tube reactor (13 mm OD × 10 mm ID × 220 mm long). The catalyst was pretreated with an Ar stream (20 mL min<sup>-1</sup>) at 750 °C (10 °C min<sup>-1</sup>) for 30 min to remove moisture. The catalyst was then carbonized at 750 °C using a 10% Ar/CH<sub>4</sub> stream (20 mL min<sup>-1</sup>) for 15 min to

transform MoO<sub>3</sub> into MoC<sub>x</sub>. The carbonized catalysts were denoted as xMoC<sub>x</sub>/Al<sub>2</sub>O<sub>3</sub>. After carbonization, 10 mL min<sup>-1</sup> of mixed gases, including 45% CH<sub>4</sub>, 45% N<sub>2</sub>, and 10% Ar (the internal standard), were admitted to the system and allowed to react for 6 h. The outlet products were separated and analyzed using an online gas chromatograph (GC, SRI 8610C) equipped with a flame ionization detector (FID) and a thermal conductivity detector (TCD) for quantification. A PoraPLOT Q-HT capillary column (25 m × 0.53 mm × 20 μm) was used for separation. The CH<sub>4</sub> conversion (%) and turnover frequency of each product (TOF, h<sup>-1</sup>) were calculated based on the observable products by using the following equations:

$$\text{CH}_4 \text{ conversion (\%)} = \frac{\sum [(\text{C atoms in product}) \times F_{\text{product}}]}{F_{\text{methane}}} \times 100 \quad (1)$$

$$\text{TOF (h}^{-1}\text{)} = \frac{(\text{C atoms in product}) \times F_{\text{product}}}{(\text{Mo mole in catalyst bed}) \times (\text{dispersion})} \quad (2)$$

“C atoms in product” is the carbon number of each product.  $F_{\text{product}}$  is the molar flow rate (μmol h<sup>-1</sup>) of the product at the outlet stream.  $F_{\text{methane}}$  is the molar flow rate of CH<sub>4</sub> (μmol h<sup>-1</sup>) at the inlet stream.

## Results and discussion

### Characterization

The bulk structure of the catalysts was determined by XRD, XAS at the Mo *K*-edge, and TEM, as shown in Fig. 3. The diffraction patterns of all Al<sub>2</sub>O<sub>3</sub>-supported MoC<sub>x</sub> catalysts were similar to that of the pristine Al<sub>2</sub>O<sub>3</sub> (Fig. 3a), indicating the presence of well-dispersed Mo<sub>2</sub>C or Mo<sub>2</sub>C crystals that are undetectable by XRD. Unsupported Mo<sub>2</sub>C prepared by carbonization had similar diffraction to that of com-Mo<sub>2</sub>C (Fig. S1†), confirming that the Mo<sub>2</sub>C phase is successfully synthesized. Fig. 3b shows the Mo *K*-edge XAS spectra of the tested catalysts. Mo foil, Mo<sub>2</sub>C, MoO<sub>3</sub>, and 1MoC<sub>x</sub>/Al<sub>2</sub>O<sub>3</sub> were included for reference. The absorption edge shows an increasing trend as follows: Mo foil (20 003.9 eV) < Mo<sub>2</sub>C (20 010.9 eV) < 1MoC<sub>x</sub>/Al<sub>2</sub>O<sub>3</sub> (20 012.2 eV) < 5MoC<sub>x</sub>/Al<sub>2</sub>O<sub>3</sub> (20 013.7 eV) < 10MoC<sub>x</sub>/Al<sub>2</sub>O<sub>3</sub> (20 015.5 eV) < 1MoO<sub>3</sub>/Al<sub>2</sub>O<sub>3</sub> (20 015.8 eV) = MoO<sub>3</sub> (20 015.8 eV), indicating the increasing oxidation state of Mo species. Moreover, the linear combination result of each XAS spectrum (see Fig. 3c) by using Mo<sub>2</sub>C and MoO<sub>3</sub> as representatives showed that the composition of Mo<sub>2</sub>C decreased following the order 1MoC<sub>x</sub>/Al<sub>2</sub>O<sub>3</sub> (73.4%) > 5MoC<sub>x</sub>/Al<sub>2</sub>O<sub>3</sub> (56.0%) > 10MoC<sub>x</sub>/Al<sub>2</sub>O<sub>3</sub> (20.0%). This fitted result suggested that the Mo<sub>2</sub>C phase is formed after carbonization and is dominant in 1MoC<sub>x</sub>/Al<sub>2</sub>O<sub>3</sub>.

The dark-field TEM images (Fig. 3d, g, and j) do not reveal any distinct Mo particles, likely because of the presence of small and evenly dispersed Mo particles. The Mo La mapping images (Fig. 3e, h, and k) confirm that

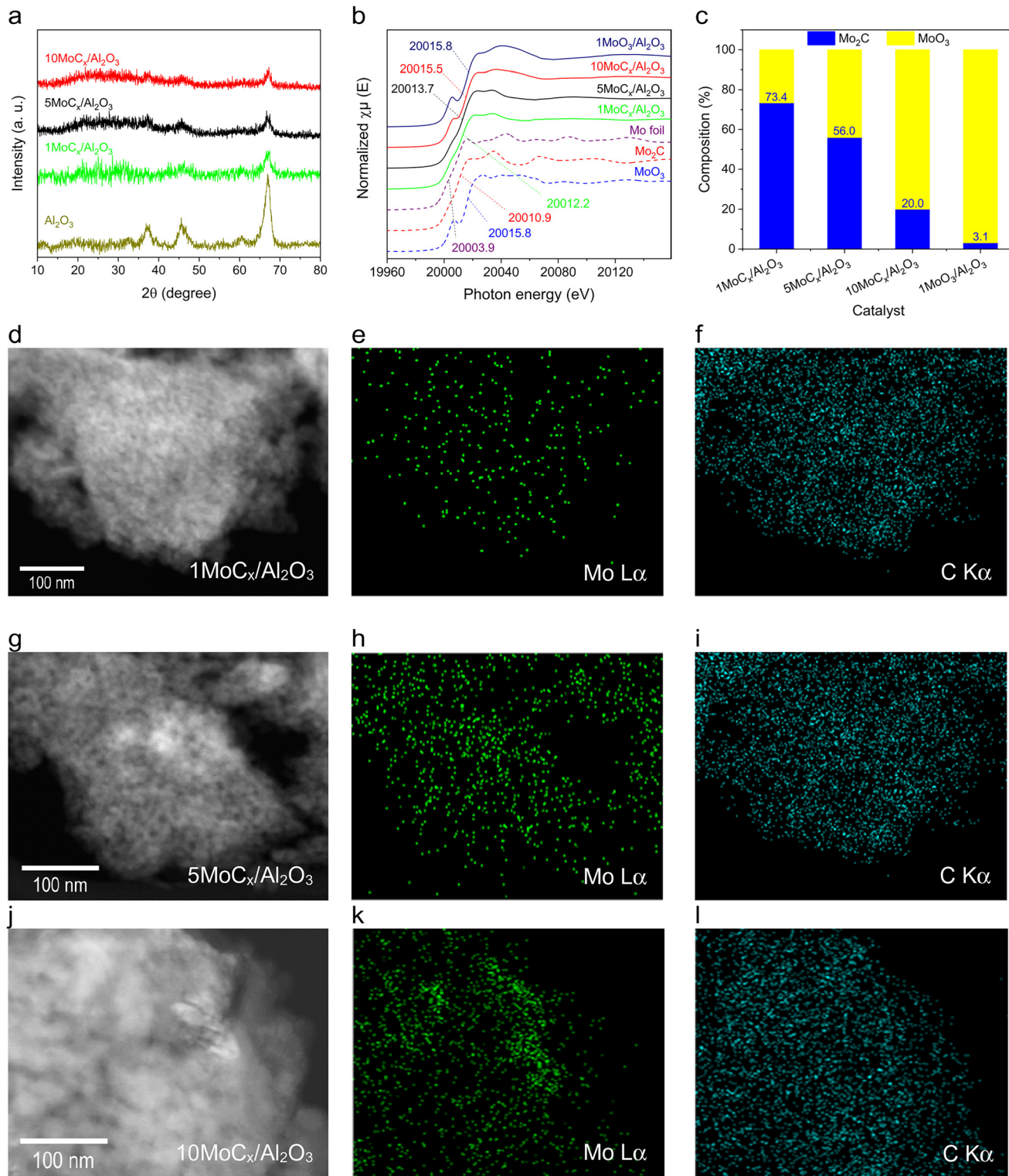


**Fig. 3** (a) XRD patterns of  $\text{Al}_2\text{O}_3$  and tested catalysts, (b) XAS spectra, and (c) linear combination fitting (LCF) results of supported  $\text{MoCx}$  catalysts.  $\text{MoO}_3$ ,  $\text{Mo}_2\text{C}$ , Mo foil, and  $1\text{MoO}_3/\text{Al}_2\text{O}_3$  were included as the standards. Representative dark-field TEM images of (d)  $1\text{MoCx}/\text{Al}_2\text{O}_3$ , (g)  $5\text{MoCx}/\text{Al}_2\text{O}_3$ , and (j)  $10\text{MoCx}/\text{Al}_2\text{O}_3$  and their EDS mapping results at Mo L $\alpha$  and C K $\alpha$ . (e) and (f) show the EDS mappings of  $1\text{MoCx}/\text{Al}_2\text{O}_3$ ; (h) and (i)  $5\text{MoCx}/\text{Al}_2\text{O}_3$ ; (k) and (l)  $10\text{MoCx}/\text{Al}_2\text{O}_3$ .

Mo is uniformly distributed. Notably, even for  $10\text{MoCx}/\text{Al}_2\text{O}_3$ , no aggregated Mo clusters were observed. Moreover, the C K $\alpha$  images (Fig. 3f, i, and l) indicated a higher

concentration of carbon species than that of Mo in each catalyst, suggesting the coexistence of deposited carbon species with carbides.

**Table 1** Physicochemical properties of  $\text{Al}_2\text{O}_3$ -supported  $\text{Mo}_2\text{C}$  catalysts

Catalyst	Mo loading <sup>a</sup> (%)	Surface area <sup>b</sup> ( $\text{m}^2 \text{ g}^{-1}$ )	Pore volume <sup>c</sup> ( $\text{cm}^3 \text{ g}^{-1}$ )	Dispersion <sup>d</sup> (%)	Acidity <sup>e</sup> ( $\mu\text{mol g}^{-1}$ )
$1\text{MoC}_x/\text{Al}_2\text{O}_3$	1.01	139	0.32	17.8	469
$5\text{MoC}_x/\text{Al}_2\text{O}_3$	4.74	95	0.24	8.5	393
$10\text{MoC}_x/\text{Al}_2\text{O}_3$	9.99	39	0.22	2.1	172

<sup>a</sup> Determined by ICP-MS. <sup>b</sup> Estimated by the BET method. <sup>c</sup> Calculated by the BJH method. <sup>d</sup> Obtained by CO pulse titration. <sup>e</sup> Evaluated by the  $\text{NH}_3$ -TPD technique.

The physicochemical properties of  $\text{Al}_2\text{O}_3$ -supported  $\text{MoC}_x$  catalysts are listed in Table 1. The Mo content of each catalyst is close to its designated value. The  $\text{N}_2$  isotherms of all catalysts showed a type IV isotherm and H1 hysteresis loop, indicating the presence of a mesoporous structure (Fig. S2†).<sup>30,31</sup> The surface areas of the tested catalysts varied in the range of 39 to  $139 \text{ m}^2 \text{ g}^{-1}$  and they exhibited a pore volume of  $0.22\text{--}0.32 \text{ cm}^3 \text{ g}^{-1}$ . The surface area and pore volume decreased with increasing Mo loading. This is likely due to the occupation of accessible pores by Mo species, making gas adsorption difficult.<sup>32</sup> Hence, a higher Mo loading would lead to more available pores being occupied, resulting in a reduced gas adsorption capacity.

The dispersion of  $\text{MoC}_x$  decreased with increasing Mo loading. As seen from the TEM images, the  $\text{Mo}_2\text{C}$  particle size was increased with increasing Mo loading. The increased particle size indicated a higher degree of  $\text{Mo}_2\text{C}$  agglomeration, which reduced the surface-to-volume ratio of  $\text{Mo}_2\text{C}$ . Therefore, the surface availability of  $\text{Mo}_2\text{C}$  at a high Mo content is suppressed. The total acidity of the  $\text{Al}_2\text{O}_3$ -supported  $\text{Mo}_2\text{C}$  catalysts also decreased when the Mo loading was increased (Fig. S3†).  $\text{Al}_2\text{O}_3$  exhibits Lewis acidity, whereas  $\text{Mo}_2\text{C}$  has Lewis basic sites.<sup>33</sup> By adjusting the Mo loading, it becomes possible to occupy the acidic sites of  $\text{Al}_2\text{O}_3$ , leading to a decrease in acidity. The coverage of acid sites increases with higher Mo loading.

### Catalytic evaluation

$\text{CH}_4$  conversion was tested in either a  $\text{N}_2$  or Ar stream to verify that gaseous  $\text{N}_2$  is activated and reacted with  $\text{CH}_4$  to form ACN. Similar profiles of  $\text{CH}_4$  conversion and TOF of hydrocarbons (ethylene, ethane, benzene, and toluene) were observed in both  $\text{N}_2$  (closed squares) and Ar (open circles) streams (Fig. 4a and S4†). This indicated that the  $\text{N}_2$  and Ar atmospheres had little influence on the transformation of  $\text{CH}_4$  into hydrocarbons. Moreover, it can be seen that the  $\text{CH}_4$  conversion and TOF of hydrocarbons decreased synchronously with time, indicating that the active sites for hydrocarbon formation are deactivated, likely due to coke accumulation.<sup>34</sup>

Note that ACN production was solely observed when  $\text{CH}_4$  was converted in  $\text{N}_2$  (Fig. 4a). That is,  $\text{N}_2$  activation and N-insertion took place in  $\text{CH}_4$  conversion. Since gaseous  $\text{N}_2$  is the sole N-containing reagent, the formation of ACN could be attributed to gaseous  $\text{N}_2$  activation. To further clarify that ACN

can be produced in the presence of  $\text{N}_2$ ,  $\text{N}_2\text{--Ar--N}_2$  (Fig. 4b) and  $\text{Ar--N}_2\text{--Ar}$  (Fig. 4c) switching tests were conducted. Again, operating in varying streams has a negligible impact on the  $\text{CH}_4$  conversion (black scatters in Fig. 4b and c). In the  $\text{N}_2\text{--Ar--N}_2$  switching test (Fig. 4b), the TOF of ACN was initially high ( $13.0 \text{ h}^{-1}$ ) when operating under  $\text{N}_2$  (red closed squares). After switching to Ar (red open circles), the TOF of ACN decreased sharply, indicating that ACN cannot be produced in Ar. When the reaction stream was switched back to  $\text{N}_2$ , the TOF recovered to  $8.2 \text{ h}^{-1}$  (red closed squares), underlining that ACN is produced by feeding  $\text{N}_2$ . Comparatively, in the  $\text{Ar--N}_2\text{--Ar}$  switching test (Fig. 4c), there was no ACN produced at the beginning of the test when feeding Ar (red open circles). After switching the feed to  $\text{N}_2$ , a significant increase in the TOF of ACN was observed ( $6.1 \text{ h}^{-1}$ , red closed squares), emphasizing that  $\text{N}_2$  activation occurs, which can react with  $\text{CH}_4$  to form ACN. However, ACN could still be produced when  $\text{N}_2$  was replaced by Ar (red open circles). Presumably, there is deposited carbon on the  $\text{MoC}_x$  surface during the first cycle in Ar. After purging  $\text{N}_2$ , the converted  $\text{N}_2$  could also react with the  $\text{MoC}_x$  surface, forming a carbonitride-like structure.<sup>35</sup> This structure is proposed to act as a N-source for ACN synthesis. It can be concluded at this stage that  $\text{Al}_2\text{O}_3$ -supported  $\text{MoC}_x$  is active for the co-activation of  $\text{CH}_4$  and  $\text{N}_2$ , and ACN can be produced merely in  $\text{N}_2$ .

The effects of operating temperature (650, 700, 750, and  $800^\circ\text{C}$ ) and Mo loading (1, 5, and 10 wt%) were evaluated for the conversion of  $\text{CH}_4$  using the  $\text{MoC}_x/\text{Al}_2\text{O}_3$  catalysts (Table 2, entries 1–4 and Fig. S5†).  $\text{Mo}_2\text{C}$  and  $\text{MoO}_3$  were tested, and both showed negligible activities. The  $\text{CH}_4$  conversion is increased with temperature from 9.3% ( $650^\circ\text{C}$ ) to 25.0% ( $800^\circ\text{C}$ ). The TOFs of  $\text{C}_2$  species and coke also increased with reaction temperature. However, aromatics reached the highest TOF at  $750^\circ\text{C}$  and then declined. This is likely caused by the over-oligomerization of aromatics to form coke. The TOF of ACN also increased with reaction temperature, suggesting the progressively enhanced extent of C–H bond and  $\text{N}\equiv\text{N}$  bond cleavages. At  $800^\circ\text{C}$ , the TOF of ACN was high at the beginning of the reaction, but showed a rapidly decreasing trend. Hence, a temperature of  $750^\circ\text{C}$  was selected for further investigations.

In addition to determining the effect of reaction temperature,  $\text{CH}_4$ -TPSR experiments were also conducted, as shown in Fig. S6.†  $\text{CH}_4$  ( $m/z = 16$ ) started to be converted at  $640^\circ\text{C}$  with a maximum conversion rate at  $730^\circ\text{C}$ .

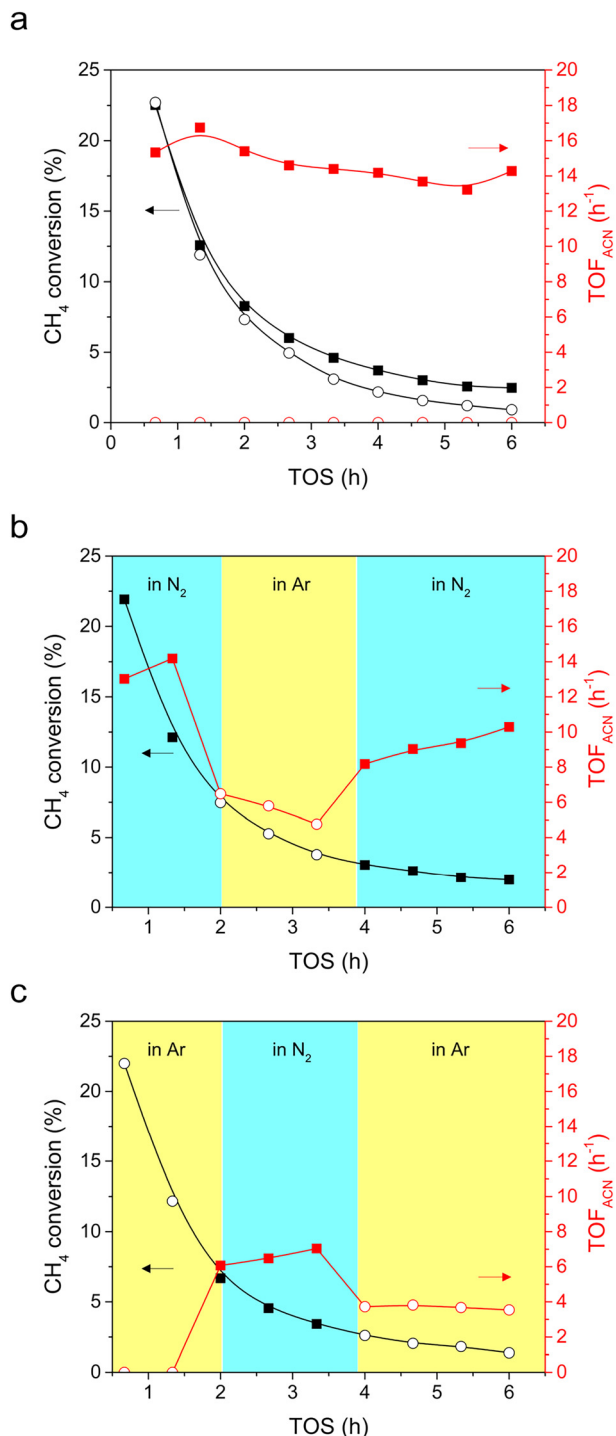


**Fig. 4** Time on stream (TOS) profiles of (a)  $\text{CH}_4$  conversion (black) and TOF of ACN (red) under  $\text{N}_2$  (closed squares) and Ar (open circles) atmospheres and the TOS profiles of  $\text{CH}_4$  conversion and TOF of ACN during the (b)  $\text{N}_2$ -Ar- $\text{N}_2$  and (c) Ar- $\text{N}_2$ -Ar switching tests. Reaction conditions: 0.18 g of  $1\text{MoC}_x/\text{Al}_2\text{O}_3$ , reaction temperature = 750 °C, GHSV = 1500  $\text{mL}_{\text{CH}_4} \text{g}_{\text{cat}}^{-1} \text{h}^{-1}$ , feed = 4.5/4.5/1  $\text{mL min}^{-1}$  of  $\text{CH}_4/\text{N}_2/\text{Ar}$  or 4.5/5.5  $\text{mL min}^{-1}$  of  $\text{CH}_4/\text{Ar}$ .

°C. The onset temperatures of major products, including ACN ( $m/z = 41$ ),  $\text{C}_2$  species ( $m/z = 29$ ), and benzene ( $m/z = 78$ ), were approximately 650 °C. Therefore, it could be

suggested that the formation reactions of ACN and hydrocarbons proceed in parallel.

The effect of Mo loading (Table 2, entries 3, 5, and 6 and Fig. S7†) was tested at a 750 °C. The  $\text{CH}_4$  conversion and TOF of  $\text{C}_2$  and aromatics decreased with increasing Mo loading. This is likely due to the suppressed acidity at a high Mo loading since C-H activation is promoted by acidic sites.<sup>36,37</sup> The TOF of ACN had negligible change with respect to the Mo loading. However, a small amount of HCN could be observed when the Mo loading is higher than 5%. Moreover,  $1\text{MoC}_x/\text{Al}_2\text{O}_3$  exhibited the most stable TOF of ACN during the 6 h testing. Accordingly,  $1\text{MoC}_x/\text{Al}_2\text{O}_3$  was further investigated.

In comparison, the equilibrium conversion of  $\text{CH}_4$  and  $\text{N}_2$  to ACN ( $2\text{CH}_4 + 0.5\text{N}_2 \leftrightarrow \text{CH}_3\text{CN} + 2.5\text{H}_2$ ) was performed from 300 °C to 1000 °C using ThermoSolver. The obtained parameters are presented in Table S1.† It can be seen that the equilibrium constant ( $K_{\text{eq}}$ ) increases with increasing temperature, indicating the endothermic nature of  $\text{CH}_4$  conversion to ACN. However, the values of  $K_{\text{eq}}$  at all tested temperatures are very small. That is, the reaction is highly unpreferable, in which low  $\text{CH}_4$  and  $\text{N}_2$  conversions and a low ACN yield were expected. The equilibrium  $\text{CH}_4$  conversion as a function of temperature is illustrated in Fig. S8.† At 750 °C, only 0.55% of  $\text{CH}_4$  is converted in the equilibrium state. Note that using a  $\text{MoC}_x$ -based catalyst resulted in approximately 1.5%  $\text{CH}_4$  conversion, suggesting the effectiveness of  $\text{Mo}_2\text{C}$  in the cleavage of C-H and N≡N bonds.

The above activity results showed that the major products were aromatics and coke, possibly due to the strong interaction between  $\text{Mo}_2\text{C}$  nanoparticles and  $\text{CH}_4$ .<sup>38</sup> Moreover, a parallel reaction pathway to produce ACN and hydrocarbons was suggested by the similar onset temperature from  $\text{CH}_4$ -TPSR. One way to suppress aromatization and coke is through co-feeding hydrogen in the reactant stream.<sup>39</sup> Hence, the effect of co-feeding  $\text{H}_2$  (10, 20, 25, and 33% v/v) was investigated at 750 °C by using  $1\text{MoC}_x/\text{Al}_2\text{O}_3$  (see Fig. 5 and S9†). Co-feeding  $\text{H}_2$  varies the concentration of  $\text{CH}_4$  which can affect reactivity. Accordingly, using Ar as a diluent with the same concentration as that of  $\text{H}_2$  was also investigated to validate that the activity is not only affected by the low  $\text{CH}_4$  concentration.

The initial  $\text{CH}_4$  conversion and TOFs of hydrocarbons ( $\text{C}_2$  and aromatics) and ACN decreased with increasing concentration of diluent. In addition, the initial  $\text{CH}_4$  conversion and TOFs under the  $\text{H}_2$  stream (magenta bars) were more strongly influenced than those tested in the Ar stream (yellow bars), in which aromatics are the most affected species (see Fig. 5d). In other words,  $\text{H}_2$  co-feeding does not only dilute the concentration of  $\text{CH}_4$  but also dampens the aromatization activity. Moreover, after 12 h on stream, the  $\text{CH}_4$  conversion decreased severely in the Ar stream (22.5%, 19.6%, 18.1%, and 13.7% declined to 0.6%, 0.8%, 0.5%, and 0.4% at 10, 20, 25, and 33% Ar concentration, respectively), compared to those in the  $\text{H}_2$  co-

**Table 2** Catalytic activity testing for  $\text{CH}_4$  conversion over the  $\text{Al}_2\text{O}_3$ -supported  $\text{MoC}_x$  catalysts. Reaction conditions: 0.18 g catalyst, 10  $\text{mL min}^{-1}$  of the feed mixture

Entry	Catalyst	Temp. (°C)	$\text{CH}_4$ conversion <sup>a</sup> (%)	TOF <sup>a</sup> (h <sup>-1</sup> )				
				$\text{C}_2$	Aromatics	ACN	HCN	Coke <sup>b</sup>
1	1 $\text{MoC}_x/\text{Al}_2\text{O}_3$	650	9.3 (5.5)	8.6 (5.1)	65.0 (23.3)	1.1 (6.3)	N/D	23.2
2		700	17.2 (6.0)	16.6 (9.6)	123.7 (14.7)	5.1 (9.5)	N/D	26.7
3		750	26.1 (6.0)	30.7 (8.4)	168.8 (1.0)	15.3 (14.3)	N/D	33.6
4		800	25.0 (8.4)	38.6 (11.9)	109.5 (0.5)	20.8 (5.5)	N/D	58.2
5	5 $\text{MoC}_x/\text{Al}_2\text{O}_3$	750	26.5 (5.9)	13.5 (2.3)	72.2 (0.1)	7.8 (4.6)	1.2 (0)	18.1
6	10 $\text{MoC}_x/\text{Al}_2\text{O}_3$		15.4 (3.0)	15.2 (3.1)	80.3 (0.0)	13.2 (5.9)	2.1 (0)	15.3

<sup>a</sup> Data were taken from the TOS profiles at 40 min and 6 h (shown in brackets). <sup>b</sup> Average coke formation rate, determined by TGA.

fed stream (20.0%, 10.1%, 5.6%, and 1.2% decreased to 4.6%, 4.1%, 2.5%, and 1.0% at 10, 20, 25, and 33%  $\text{H}_2$  concentration, respectively). This implied that the reactivity is more stable when  $\text{H}_2$  is present.

As seen by the TOFs at 12 h on stream (Fig. 5b-d), the products were still producible in the  $\text{H}_2$  atmosphere, while there were almost no products formed under the Ar stream at the 12th hour. Accordingly, it could be claimed that gaseous  $\text{H}_2$  also reduces the amount of carbon deposits on the catalyst surface, resulting in a steadier reactivity.<sup>39</sup>

XPS spectra of the  $\text{Mo}_2\text{C}$  and  $1\text{MoC}_x/\text{Al}_2\text{O}_3$  catalysts are illustrated in Fig. 6. The photoline of  $\text{Mo}_2\text{C}$  at Mo 3d (Fig. 6a) could be deconvoluted into five responses. The responses at 235.8 and 232.7 eV are attributed to  $\text{Mo}^{6+}$  (red);<sup>40</sup> 229.5 eV,  $\text{Mo}^{3+}$  (magenta);<sup>41</sup> 231.3 and 228.4 eV,  $\text{Mo}^{2+}$  (blue).<sup>42</sup> The presence of  $\text{Mo}^{2+}$  signals indicated the existence of  $\text{Mo}_2\text{C}$  species, while  $\text{Mo}^{6+}$  and  $\text{Mo}^{3+}$  could be assigned as  $\text{MoO}_3$  and  $\text{Mo}_2\text{O}_3$ , respectively. The existence of oxidic species could be attributed to the oxidation of the  $\text{Mo}_2\text{C}$  surface.<sup>43,44</sup> The spectrum of  $1\text{MoC}_x/\text{Al}_2\text{O}_3$  also contained these signals. In addition, another response at

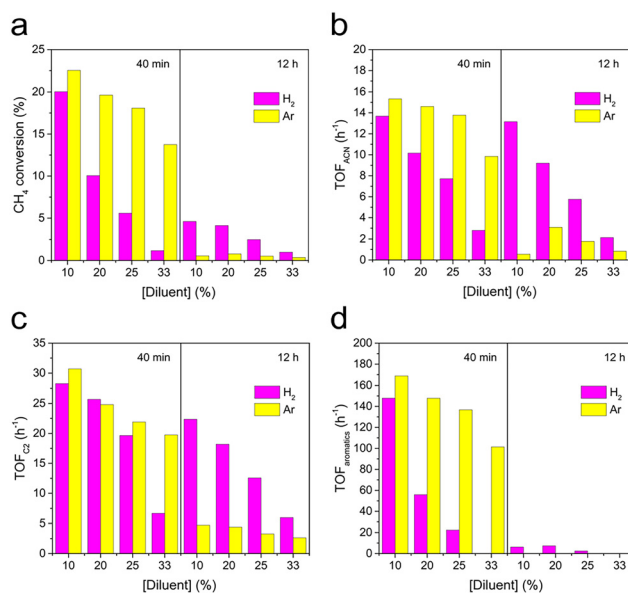
234.4 eV assigned to  $\text{Mo}^{4+}$  species<sup>45</sup> (cyan) was observed over the  $1\text{MoC}_x/\text{Al}_2\text{O}_3$  catalyst, which could be referred to the presence of MoC species, likely due to the over-carbonization of small  $\text{Mo}_2\text{C}$  particles. Oxidic molybdenum species were observed, even though the catalyst was *in situ* carbonized prior to the reaction without exposure to the atmosphere. Therefore, it could be stated that the active phase is composed of carbidic molybdenum species.

The C 1s spectra (Fig. 6b) of both  $\text{Mo}_2\text{C}$  and  $1\text{MoC}_x/\text{Al}_2\text{O}_3$  could be deconvoluted into four species, including adventitious carbon (C-C, red) at 285.0 eV, C-O (cyan) at 285.6 eV,<sup>46</sup> C=O (magenta) at 288.0 eV,<sup>47</sup> and C-Mo (blue) at 283.7 eV,<sup>48</sup> respectively. According to the characterization results, it can be concluded that the active sites of the catalysts are predominantly made of the carbide phase.

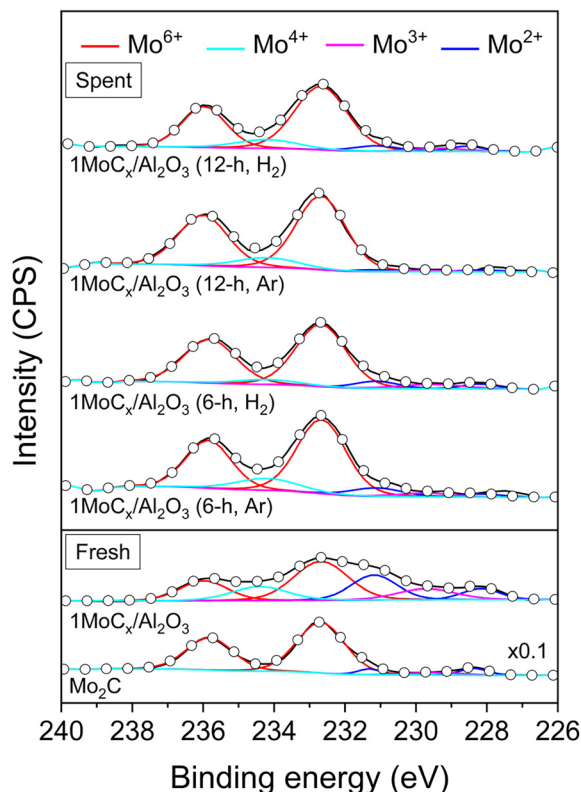
Table S2† shows the percentage of each Mo and C species obtained from the aforementioned XPS results.  $1\text{MoC}_x/\text{Al}_2\text{O}_3$  contained 28.1%  $\text{Mo}_2\text{C}$  ( $\text{Mo}^{2+}$ ) phase. Additionally, by including all carbide species ( $\text{MoC}$ ,  $\text{Mo}^{4+}$ ), the relative composition of  $\text{MoC}_x$  for  $1\text{MoC}_x/\text{Al}_2\text{O}_3$  is 43.7%, which is much higher than that of its unsupported counterpart (7.4%). This is presumably due to the presence of smaller molybdenum particles that lead to a more rapid and complete carbonization. After the reaction, the C-Mo signals were not observed. The percentage of C-C increased together with the appearance of sharper C 1s signals over the spent catalysts. This suggested the formation of graphitic carbon that dominates the signals at a similar region.<sup>49</sup>

It can be seen in Table S2† that the surface C/Mo ratios of fresh, 6 h spent (Ar), 6 h spent ( $\text{H}_2$ ), 12 h spent (Ar), and 12 h spent ( $\text{H}_2$ )  $1\text{MoC}_x/\text{Al}_2\text{O}_3$  are 1.04, 5.66, 5.56, 11.23, and 6.78, respectively. It has been reported that the reactivity of molybdenum carbides depends on the C/Mo ratio, in which the catalyst with a lower C/Mo ratio is more reactive.<sup>38</sup> In this case, the C/Mo ratio rapidly increased when the reaction was performed in the Ar atmosphere (from 1.04 (fresh) to 5.66 (6 h, Ar) to 11.23 (12 h, Ar)), while it was more stable in the  $\text{H}_2$  stream (from 1.04 (fresh) to 5.56 (6 h,  $\text{H}_2$ ) to 6.78 (12 h,  $\text{H}_2$ )). Accordingly, the enhanced stability of  $\text{CH}_4$  conversion and TOF is likely related to the more consistent surface C/Mo ratio achieved when  $\text{H}_2$  is present.

The TOF of ACN and  $\text{C}_2$  was more stable when co-feeding  $\text{H}_2$ . Additionally, it can be seen that the TOF of

**Fig. 5** Effects of  $\text{H}_2$  co-feeding and Ar dilution on (a)  $\text{CH}_4$  conversion and TOF of (b) ACN, (c)  $\text{C}_2$ , and (d) aromatics by using  $1\text{MoC}_x/\text{Al}_2\text{O}_3$ .

a



b

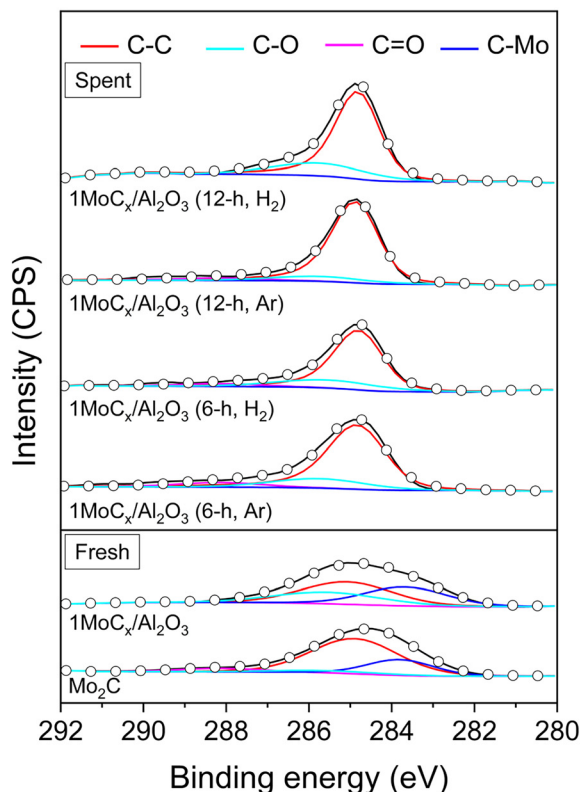


Fig. 6 XPS spectra of fresh and spent MoCx catalysts for (a) Mo 3d and (b) C 1s.

aromatics is suppressed by ~87% at 25% H<sub>2</sub>. When the concentration of H<sub>2</sub> is further increased to 33%, no aromatics can be initially found. Note that the CH<sub>4</sub> conversion under these conditions is almost negligible, which explains the disappearance of aromatics. Therefore, 25% H<sub>2</sub> was selected for 50 h stability testing.

Fig. 7 shows that the on-stream activity was nearly unchanged in the 50 h duration test, underlining the stability of the reaction process. The CH<sub>4</sub> conversion was maintained

at approximately 2.5%. Moreover, three major products, including ACN, ethylene, and ethane, were also sustainably produced at a TOF of approximately 6.5 h<sup>-1</sup>. Aromatics and HCN were observed as by-products at a TOF of ~2.5 h<sup>-1</sup>. Therefore, the presence of 25% H<sub>2</sub> can not only suppress CH<sub>4</sub> aromatization but also enhance the stability of the catalyst during the 50 h durability test.

### Proposed mechanism

Our earlier work claimed that ACN is formed *via* surface CN species over GaN catalysts. The surface CN species are formed by reacting CH<sub>4</sub> with mobile-N of GaN at the surface.<sup>50</sup> Therefore, CN species may also form over the MoCx surface by N<sub>2</sub> cleavage. Hence, *in situ* DRIFTS experiments were performed under a N<sub>2</sub> atmosphere, as shown in Fig. S10.<sup>†</sup> Regrettably, no CN vibrational band (~2220 cm<sup>-1</sup>) could be observed. This might be attributed to (i) the high instability of evolved intermediates or (ii) no interaction being formed between N<sub>2</sub> and surface carbon of MoCx. The latter could be clarified by performing N<sub>2</sub>-H<sub>2</sub> co-feeding experiments. In the N<sub>2</sub>-H<sub>2</sub> co-feeding test, HCN should be generated if N<sub>2</sub> and surface carbon react since the surface carbon of MoCx acts similarly to surface oxygen in the Mars-van Krevelen mechanism.<sup>51,52</sup> However, no HCN could be generated (not shown), indicating that the surface carbon has

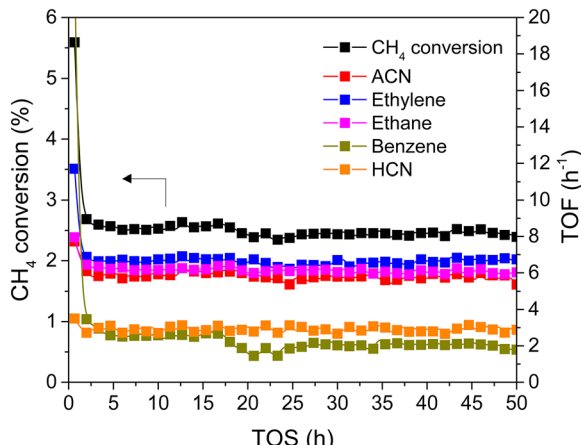


Fig. 7 50 h stability testing at 25% H<sub>2</sub> co-feeding over 1MoCx/Al<sub>2</sub>O<sub>3</sub>.

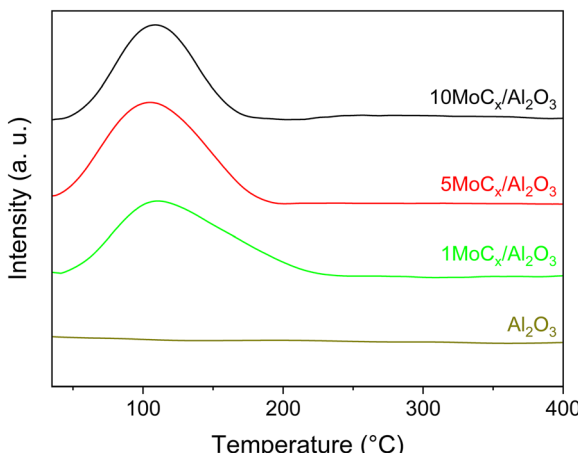


Fig. 8  $\text{N}_2$ -TPD profiles of  $\text{Al}_2\text{O}_3$ -supported  $\text{MoCx}$  catalysts and unsupported  $\text{Al}_2\text{O}_3$ .

no interaction with gaseous  $\text{N}_2$ . Nevertheless, the aforementioned results showed that ACN could be generated in which the only N-source is  $\text{N}_2$ . That is, the  $\text{N}\equiv\text{N}$  triple bond of  $\text{N}_2$  is activated. We conducted  $\text{N}_2$ -TPD to further confirm that  $\text{N}_2$  can be adsorbed on the  $\text{Al}_2\text{O}_3$ -supported  $\text{MoCx}$ . As shown in Fig. 8, the desorption peak of  $\text{N}_2$  over the  $\text{Al}_2\text{O}_3$ -supported  $\text{MoCx}$  catalysts is located at approximately  $107\text{ }^\circ\text{C}$ , while no  $\text{N}_2$  desorption can be observed over bare  $\text{Al}_2\text{O}_3$ . This implies that  $\text{N}_2$  should be firstly adsorbed on the  $\text{MoCx}$  surface and then desorbed. Considering no interaction between  $\text{N}_2$  and surface carbon (C sites) of  $\text{MoCx}$ , it can be inferred that  $\text{N}_2$  adsorption occurs on metal (Mo) sites.<sup>53–56</sup>

To clarify, the CO and  $\text{N}_2$  uptakes were compared since CO is stoichiometrically adsorbed on Mo sites.<sup>57</sup> As shown in Table S3, the CO and  $\text{N}_2$  uptakes were nearly identical for the tested catalysts. This indicated that the adsorption behaviors of CO and  $\text{N}_2$  are similar. Accordingly, it can be concluded that the adsorption of  $\text{N}_2$  takes place at the Mo sites.

Although  $\text{N}_2$  activation by  $\text{MoCx}$  was elucidated, the formation of the  $\text{C}\equiv\text{N}$  bond and ACN is still unclear. A previous study revealed that  $\text{CH}_4$  tends to be completely dissociated on Mo sites exposed on the  $\text{MoCx}$  surface.<sup>58</sup> The  $\text{MoCx}$  surface could be further carburized by the dissociated carbon adatoms diffusing into the subsurface layer, forming a MoC-like surface structure. The MoC-like surface could facilitate  $\text{CH}^*$  coupling to form  $\text{C}_2\text{H}_2^*$  as a potential intermediate.<sup>58,59</sup> The  $1\text{MoCx/Al}_2\text{O}_3$  had its C/Mo ratio estimated by XPS analysis close to unity (Table S2), similar to that of MoC. That is, the surface of  $1\text{MoCx/Al}_2\text{O}_3$  should have an MoC-like structure. Thus, we propose that the formation of ACN occurs over the Mo sites exposed on the surface of the MoC-like structure, as shown in Fig. 9.

$\text{N}_2$  could be dissociatively adsorbed on the Mo-terminated surface. Then,  $\text{CH}_4$  would be activated and dehydrogenated over the adjacent Mo sites, forming  $\text{CH}^*$  species. The  $\text{CH}^*$  species could couple with  $\text{C}_2\text{H}_2^*$  species that further react with

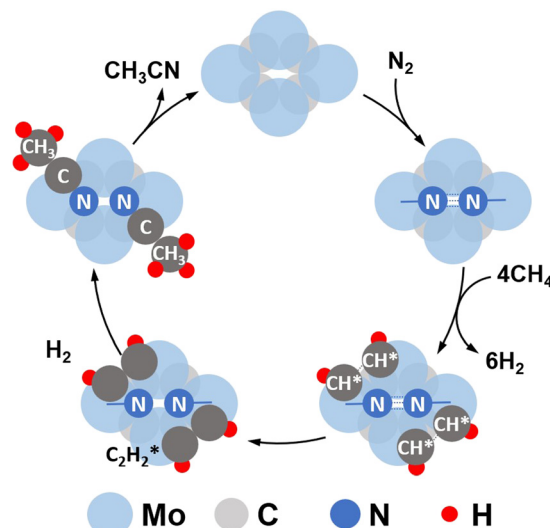


Fig. 9 Proposed co-activation of  $\text{CH}_4$  and  $\text{N}_2$  to ACN over the  $\text{MoCx}$  catalyst (top view of the catalyst surface).

N adatoms, forming ACN. The produced ACN could desorb from the surface, which fulfills the catalytic cycle.

To support this claim, kinetic analysis based on the Langmuir-Hinshelwood (LH) formalism of the proposed mechanism was performed, which is presented in the ESI. The six possible reactions were grouped into four steps, including  $\text{N}_2$  adsorption,  $\text{CH}_4$  adsorption, surface reaction, and ACN desorption. The rate expression is derived by assuming that one of the above steps is rate-limiting while the remaining steps are all in equilibrium. The rate expression was fitted to the experimental data (see Table S4) by nonlinear regression subject to minimizing the residual sum of squares to recover the values of the parameters (see Table S5). By resorting to the fitted parameters and the parity plot (Fig. S11), the surface reaction step is the most likely to occur. This result is supported by previous studies showing that the dissociative adsorption of  $\text{N}_2$  and the C-H bond cleavage of  $\text{CH}_4$  on the MoC surface are facile and unlikely to be rate-limiting.<sup>59,60</sup>

## Conclusions

In this article, two high-stability compounds ( $\text{CH}_4$  and  $\text{N}_2$ ) were simultaneously converted to form ACN over  $\text{Al}_2\text{O}_3$ -supported  $\text{MoCx}$  catalysts. ACN could only be produced in the presence of  $\text{N}_2$ , confirming the activation of the  $\text{N}\equiv\text{N}$  bond. Due to the strong interaction between  $\text{MoCx}$  and  $\text{CH}_4$ , aromatization and coking were significant, resulting in catalyst deactivation. The aromatization could be diminished by co-feeding  $\text{H}_2$ , in which the catalytic activity and TOF could be maintained for 50 h. The MoC-like surface structure of  $\text{MoCx}$  was proposed to be an active center for ACN synthesis. Kinetic analysis suggested that the surface reaction of adsorbed  $\text{N}_2$  and  $\text{C}_2\text{H}_2^*$  species is possibly the rate-determining step.

## Author contributions

Korawich Trangwachirachai: investigation, formal analysis, validation, and writing – original draft. I-Ting Kao: investigation and formal analysis. Wei-Hsiang Huang: XAS data collection and analysis. Chi-Liang Chen: XAS data collection and analysis. Yu-Chuan Lin: supervision, project administration, resources, and writing – review & editing.

## Conflicts of interest

The authors declare that they have no competing financial interests.

## Acknowledgements

This work was supported by the National Science and Technology Council (projects 109-2628-E-006-011-MY3, 110-2221-E-006-165-MY3, 110-2923-E-006-005-MY3, and 110-2927-I-006-506) and by the Higher Education Sprout Project, Ministry of Education to the Headquarters of University Advancement at National Cheng Kung University (NCKU). The authors gratefully acknowledge the use of XPS (ESCA003700) and TEM (EM000800) of NSTC 112-2740-M-006-001 belonging to the Core Facility Center of NCKU.

## References

- W. Jiang, J. Low, K. Mao, D. Duan, S. Chen, W. Liu, C. W. Pao, J. Ma, S. Sang, C. Shu, X. Zhan, Z. Qi, H. Zhang, Z. Liu, X. Wu, R. Long, L. Song and Y. Xiong, *J. Am. Chem. Soc.*, 2021, **143**, 269–278.
- P. Schwach, X. Pan and X. Bao, *Chem. Rev.*, 2017, **117**, 8497–8520.
- Z. Zhu, W. Guo, Y. Zhang, C. Pan, J. Xu, Y. Zhu and Y. Lou, *Carbon Energy*, 2021, **3**, 519–540.
- S. M. Kim, P. M. Abdala, D. Hosseini, A. Armutlulu, T. Margossian, C. Copéret and C. Müller, *Catal. Sci. Technol.*, 2019, **9**, 5745–5756.
- M. A. A. Aziz, A. A. Jalil, S. Wongsakulphasatch and D.-V. N. Vo, *Catal. Sci. Technol.*, 2020, **10**, 35–45.
- J. Niu, Y. Wang, Y. Qi, A. H. Dam, H. Wang, Y.-A. Zhu, A. Holmen, J. Ran and D. Chen, *Fuel*, 2020, **266**, 117143.
- B. C. Ekeoma, M. Yusuf, K. Johari and B. Abdullah, *Int. J. Hydrogen Energy*, 2022, **47**, 41596–41620.
- J. K. Dahl, A. W. Weimer, A. Lewandowski, C. Bingham, F. Bruetsch and A. Steinfeld, *Ind. Eng. Chem. Res.*, 2004, **43**, 5489–5495.
- Y.-R. Luo, *Comprehensive Handbook of Chemical Bond Energies*, CRC Press, 2007, p. 1688, DOI: [10.1201/9781420007282](https://doi.org/10.1201/9781420007282).
- W. Taifan and J. Baltrusaitis, *Appl. Catal., B*, 2016, **198**, 525–547.
- L. Sun, Y. Wang, N. Guan and L. Li, *Energy Technol.*, 2019, **8**, 1900826.
- D. C. Upham, V. Agarwal, A. Khechfe, Z. R. Snodgrass, M. J. Gordon, H. Metiu and E. W. McFarland, *Science*, 2017, **358**, 917–921.
- K. Dutta, V. Chaudhari, C.-J. Li and J. Kopyscinski, *Appl. Catal., A*, 2020, **595**, 117430.
- K. Trangwachirachai, C.-H. Chen and Y.-C. Lin, *Mol. Catal.*, 2021, **516**, 111961.
- K. Trangwachirachai, C.-H. Chen, A.-L. Huang, J.-F. Lee, C.-L. Chen and Y.-C. Lin, *Catal. Sci. Technol.*, 2022, **12**, 320–331.
- Z. Yuan, X. Zhang, Q. Yao, Y. Zhang and Y. Fu, *J. Anal. Appl. Pyrolysis*, 2019, **140**, 376–384.
- Future Market Insights, Acetonitrile Market, <https://www.futuremarketinsights.com/reports/acetonitrile-market>, 2023.
- A. Sieminski, *US Energy Information Administration*, 2015.
- J. J. Sattler, J. Ruiz-Martinez, E. Santillan-Jimenez and B. M. Weckhuysen, *Chem. Rev.*, 2014, **114**, 10613–10653.
- K. Trangwachirachai and Y.-C. Lin, *Dalton Trans.*, 2023, **52**, 6211–6225.
- A. Daisley and J. S. J. Hargreaves, *Catal. Today*, 2023, **423**, 113874.
- S. Tiwari, T. S. Khan, P. Tavadze and J. Hu, *Chem. Eng. J.*, 2021, **413**, 127501.
- R. Kojima and K.-I. Aika, *Appl. Catal., A*, 2001, **219**, 141–147.
- R. Michalsky, Y.-J. Zhang, A. J. Medford and A. A. Peterson, *J. Phys. Chem. C*, 2014, **118**, 13026–13034.
- H. Cheng, L.-X. Ding, G.-F. Chen, L. Zhang, J. Xue and H. Wang, *Adv. Mater.*, 2018, **30**, 1803694.
- J. Gao, Y. Zheng, G. B. Fitzgerald, J. de Joannis, Y. Tang, I. E. Wachs and S. G. Podkolzin, *J. Phys. Chem. C*, 2014, **118**, 4670–4679.
- J. Jeong, A. Hwang, Y. T. Kim, D.-Y. Hong and M.-J. Park, *Catal. Today*, 2020, **352**, 140–147.
- B. Cook, D. Mousko, W. Hoelderich and R. Zennaro, *Appl. Catal., A*, 2009, **365**, 34–41.
- B. Ravel and M. Newville, *J. Synchrotron Radiat.*, 2005, **12**, 537–541.
- S. Paganelli, R. Tassini, V. D. Rathod, B. Onida, S. Fiorilli and O. Piccolo, *Catal. Lett.*, 2021, **151**, 1508–1521.
- K. S. W. Sing and R. T. Williams, *Adsorpt. Sci. Technol.*, 2004, **22**, 773–782.
- M. J. Ramos, A. Casas, L. Rodríguez, R. Romero and Á. Pérez, *Appl. Catal., A*, 2008, **346**, 79–85.
- S. K. Bej, C. A. Bennett and L. T. Thompson, *Appl. Catal., A*, 2003, **250**, 197–208.
- C. H. L. Tempelman and E. J. M. Hensen, *Appl. Catal., B*, 2015, **176–177**, 731–739.
- P. K. Roy and S. Kumar, *ACS Appl. Energy Mater.*, 2020, **3**, 7167–7179.
- R. Gounder and E. Iglesia, *J. Am. Chem. Soc.*, 2009, **131**, 1958–1971.
- M. C. Cholewinski, M. Dixit and G. Mpourmpakis, *ACS Omega*, 2018, **3**, 18242–18250.
- M. Figueras, R. A. Gutiérrez, H. Prats, F. Viñes, P. J. Ramírez, F. Illas and J. A. Rodriguez, *Phys. Chem. Chem. Phys.*, 2020, **22**, 7110–7118.
- H. Ma, R. Kojima, S. Kikuchi and M. Ichikawa, *Catal. Lett.*, 2005, **104**, 63–66.
- C. Wu and J. Li, *ACS Appl. Mater. Interfaces*, 2017, **9**, 41314–41322.

41 Y. N. Regmi, C. Wan, K. D. Duffee and B. M. Leonard, *ChemCatChem*, 2015, **7**, 3911–3915.

42 X. Kong, S. Chen, Y. Zou, S. Lyu, X. She, Y. Lu, J. Sun, H. Zhang and D. Yang, *Int. J. Hydrogen Energy*, 2018, **43**, 13720–13726.

43 H. Vrubel and X. Hu, *Angew. Chem., Int. Ed.*, 2012, **51**, 12703–12706.

44 J. Li, C. Zhou, J. Mu, E.-C. Yang and X.-J. Zhao, *RSC Adv.*, 2018, **8**, 17202–17208.

45 H. Wei, Q. Xi, X. A. Chen, D. Guo, F. Ding, Z. Yang, S. Wang, J. Li and S. Huang, *Adv. Sci.*, 2018, **5**, 1700733.

46 L. Diao, J. Qin, N. Zhao, C. Shi, E. Liu, F. He, L. Ma, J. Li and C. He, *J. Mater. Chem. A*, 2018, **6**, 6054–6064.

47 Y. Lei, Y. Yang, Y. Liu, Y. Zhu, M. Jia, Y. Zhang, K. Zhang, A. Yu, J. Liu and J. Zhai, *Nanoscale Res. Lett.*, 2019, **14**, 329.

48 D. Wang, J. Wang, X. Luo, Z. Wu and L. Ye, *ACS Sustainable Chem. Eng.*, 2018, **6**, 983–990.

49 P. Xiao, X. Ge, H. Wang, Z. Liu, A. Fisher and X. Wang, *Adv. Funct. Mater.*, 2015, **25**, 1520–1526.

50 K. Trangwachirachai, A. L. Huang, H. K. Chen, C. L. Chen, J. F. Lee, H. K. Tian and Y. C. Lin, *Mater. Today Chem.*, 2023, **30**, 101500.

51 I. Vollmer, B. van der Linden, S. Ould-Chikh, A. Aguilar-Tapia, I. Yarulina, E. Abou-Hamad, Y. G. Sneider, A. I. O. Suarez, J.-L. Hazemann, F. Kapteijn and J. Gascon, *Chem. Sci.*, 2018, **9**, 4801–4807.

52 G. Li, I. Vollmer, C. Liu, J. Gascon and E. A. Pidko, *ACS Catal.*, 2019, **9**, 8731–8737.

53 M. Grunze, M. Golze, W. Hirschwald, H. J. Freund, H. Pulm, U. Seip, M. C. Tsai, G. Ertl and J. Küppers, *Phys. Rev. Lett.*, 1984, **53**, 850–853.

54 S. Dahl, A. Logadottir, R. C. Egeberg, J. H. Larsen, I. Chorkendorff, E. Törnqvist and J. K. Nørskov, *Phys. Rev. Lett.*, 1999, **83**, 1814–1817.

55 J. J. Mortensen, L. B. Hansen, B. Hammer and J. K. Nørskov, *J. Catal.*, 1999, **182**, 479–488.

56 W. Liao, L. Qi, Y. Wang, J. Qin, G. Liu, S. Liang, H. He and L. Jiang, *Adv. Funct. Mater.*, 2021, **31**, 2009151.

57 J. S. Lee, K. H. Lee and J. Y. Lee, *J. Phys. Chem.*, 1992, **96**, 362–366.

58 T. Zhang, X. Yang and Q. Ge, *Catal. Today*, 2021, **368**, 140–147.

59 T. Zhang, X. Yang and Q. Ge, *Catal. Today*, 2020, **339**, 54–61.

60 I. Matanovic and F. H. Garzon, *Phys. Chem. Chem. Phys.*, 2018, **20**, 14679–14687.